www.acsnano.org

Multilayered Ordered Protein Arrays Self-Assembled from a Mixed Population of Viruslike Particles

Masaki Uchida,[#] Nicholas E. Brunk,[#] Nathasha D. Hewagama, Byeongdu Lee, Peter E. Prevelige, Jr., Vikram Jadhao,* and Trevor Douglas*



Downloaded via INDIANA UNIV BLOOMINGTON on May 14, 2022 at 16:27:38 (UTC). See https://pubs.acs.org/sharingguidelines for options on how to legitimately share published articles.

Cite This: https://doi.org/10.1021/acsnano.1c11272



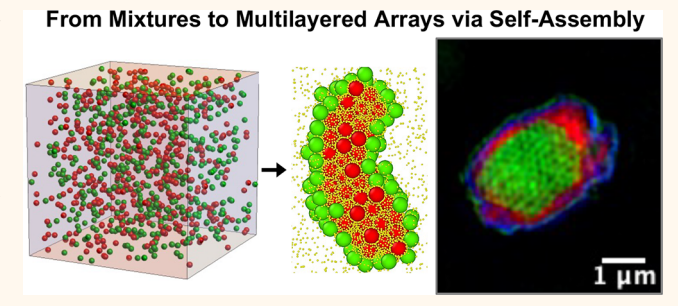
ACCESS

III Metrics & More

Article Recommendations

Supporting Information

ABSTRACT: Biology shows many examples of spatially controlled assembly of cells and biomacromolecules into hierarchically organized structures, to which many of the complex biological functions are attributed. While such biological structures have inspired the design of synthetic materials, it is still a great challenge to control the spatial arrangement of individual building blocks when assembling multiple types of components into bulk materials. Here, we report self-assembly of multilayered, ordered protein arrays from mixed populations of virus-like particles (VLPs). We systematically tuned the magnitude of the surface charge of the



VLPs via mutagenesis to prepare four different types of VLPs for mixing. A mixture of up to four types of VLPs selectively assembled into higher-order structures in the presence of oppositely charged dendrimers during a gradual lowering of the ionic strength of the solution. The assembly resulted in the formation of three-dimensional ordered VLP arrays with up to four distinct layers including a central core, with each layer comprising a single type of VLP. A coarse-grained computational model was developed and simulated using molecular dynamics to probe the formation of the multilayered, core-shell structure. Our findings establish a simple and versatile bottom-up strategy to synthesize multilayered, ordered materials by controlling the spatial arrangement of multiple types of nanoscale building blocks in a one-pot fabrication.

KEYWORDS: self-assembly, ordered protein arrays, hierarchical structures, core-shell structures, multilayered materials, virus-like particles, electrostatic interactions

iomimetic materials design and discovery often takes inspiration from the functional complexity of biological systems; nowhere is this complexity more striking than in the organization of cells in complex living organisms. Welldefined spatial segregation of cells into hierarchically organized three-dimensional (3D) structures is a critical developmental step in biological systems. Studies of developing embryos suggest that spatial segregation of cells during morphogenesis is not solely due to the chronological sequence in the developmental process. The process often involves selective adhesion of cells leading to the formation of more thermodynamically stable structures, which can be independent of the developmental sequence. For example, Townes and Holtfreter demonstrated that, when three amphibian germ layers (endoderm, mesoderm, and ectoderm) were dissociated into a mixture of individual cells, the mixture could selfassemble into their developmentally correct positions to remake the three spatially segregated germ layers in vitro.2 More recently, Foty and Steinberg showed that a mixture of

two populations of cells of the same cell type but differing in the expression levels of a cell adhesion protein (N-cadherin) segregated from each other (data reproduced in Figure S1)³ based on a reduction of the free energy of adhesion, as cells tend to maximize their mutual binding. These studies highlight the inspiration, importance, and potential of developing synthetic approaches to control the self-assembly of complex mixtures of different types of biomolecular building blocks in order to fabricate spatially segregated, multilayered hierarchical structures.

Received: December 19, 2021 Accepted: May 2, 2022



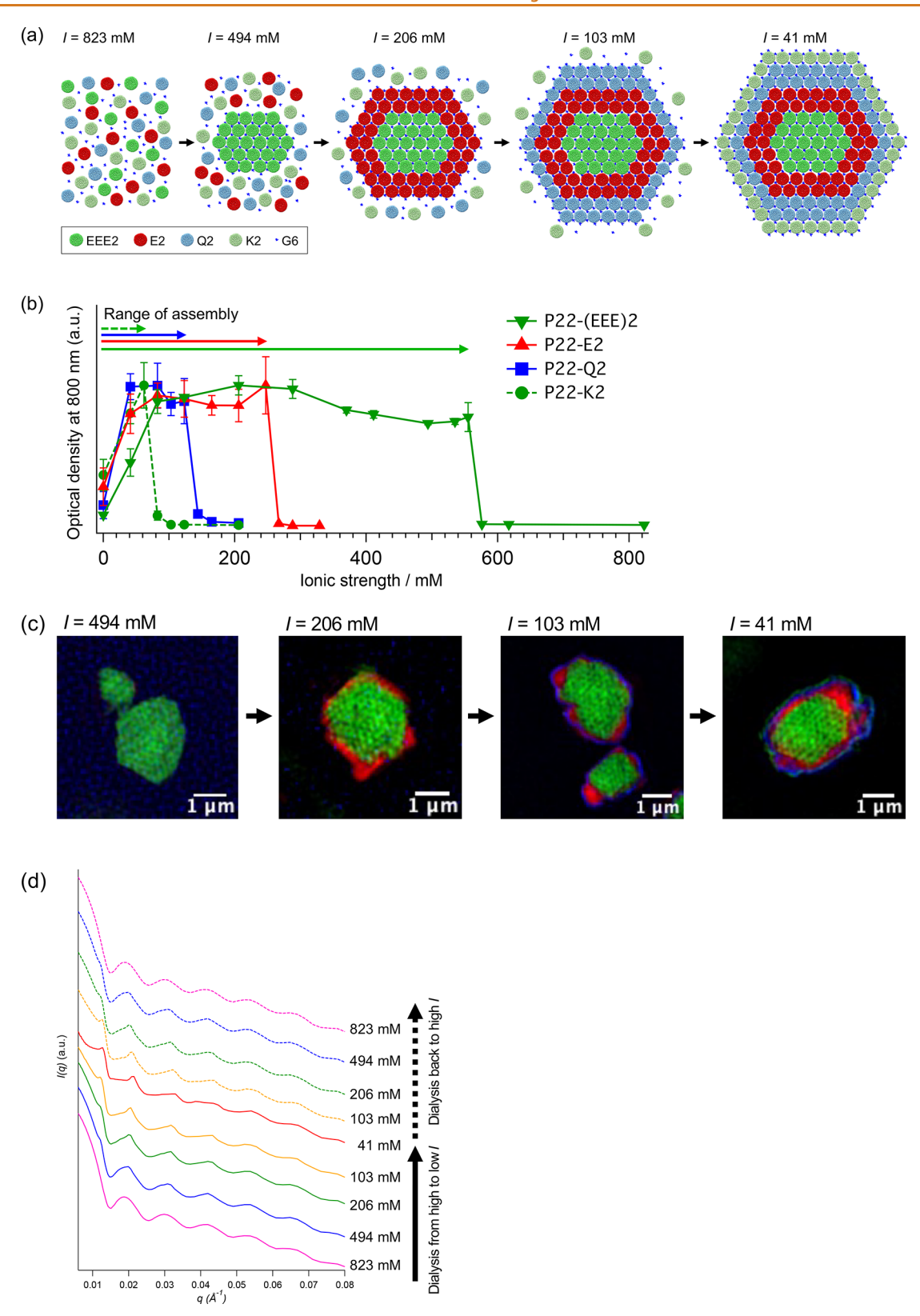


Figure 1. (a) Schematic showing assembly of multiple types of P22 VLP building blocks into an ordered core-shell array in the presence of G6 dendrimers through modulation of ionic strength by dialysis. Each VLP subpopulation assembled into an ordered array below the corresponding ionic strength threshold, leading to the formation of a multilayered hierarchical structure during dialysis through each threshold. (b) Assembly of VLPs in a one-component system, i.e., a single P22 variant in the presence of G6 dendrimers, was examined by monitoring optical density at 800 nm for a range of ionic strengths. High optical density indicates the formation of large aggregates due to light scattering. Each variant of P22 VLP exhibited different threshold ionic strengths (I_t) , above which array formation does not occur. (c) Super-resolution fluorescence microscope observation of P22 VLP arrays formed in a mixture of four types of VLPs at various steps of the dialysis process. P22-EE2, P22-E2, P22-Q2, and P22-K2 VLPs were labeled with Alexa-488, Texas Red, CF405M, and Alexa-488

ACS Nano www.acsnano.org **Article**

Figure 1. continued

fluorescent dyes, respectively. Hierarchically organized protein arrays were constructed from four types of P22 VLPs through a step-by-step dialysis from the ionic strength I = 823 to 41 mM. VLP arrays formed at I = 494 mM showed only a green fluorescent color, indicating they are composed solely of P22-EEE2 VLPs, because I is slightly below I_t^{EEE2} but much higher-than I_t^{E2} , I_t^{Q2} , and I_t^{K2} . A layer of red fluorescent color was observed on the top of the green core at I = 206 mM, suggesting that P22-E2 VLPs selectively attached on the P22-EE2 array. Similarly, thin layers of P22-Q2 and P22-K2 VLPs were formed on the existing layers at I = 103 mM and I = 41 mM, respectively. The images were acquired with a section spacing of 0.125 µm along the z-axis, and sections from the middle of the arrays are shown here. (d) Small-angle X-ray scattering (SAXS) analysis of samples containing a mixture of four types of VLPs, at each step of the dialysis process. At the starting point (I = 823 mM), only a form factor of P22 VLPs was observed, because all types of VLPs were dispersed in solution at I =823 mM. Peaks attributed to a structure factor of VLPs became more prominent as the samples were dialyzed to low ionic strength. The peaks are indicative of long-range ordering and correspond to an FCC structure. The structure factor gradually diminished as the samples were dialyzed back to high ionic strength, suggesting the disassembly of VLPs from the arrays when the ionic strength reached above the I_t of each type of VLP.

Hierarchically organized 3D assemblies of nanoscale building blocks can exhibit properties and functions beyond those of individual building blocks.⁴⁻⁶ Thus, significant effort has been devoted in recent years to establish strategies to control the bottom-up assembly of nanoscale building blocks into well-defined architectures. 7-10 Because of their diverse and sophisticated functionalities, proteins have attracted a lot of interest as building block macromolecules for constructing hierarchical 3D assemblies. 11-14 Besides conventional protein crystallization approaches, 15-20 interactions such as metal ligand coordination, 21,22 complementary DNA, 23-26 as well as electrostatic, ^{27–33} hydrophobic, ^{34,35} and specific protein protein^{36,37} interactions have been exploited to mediate the assembly of protein building blocks into ordered 3D structures. Nevertheless, it continues to be a challenge to control the spatial arrangement of two, three, or more types of building blocks while assembling them into hierarchically organized 3D architectures.

Here, we report the self-assembly of multilayered ordered arrays from a mixed population of building blocks, where each layer is populated with building blocks of the same type. Such a selective, spatially defined assembly of building blocks is achieved by modulating two material attributes: the surface charge of the building blocks and ionic strength of the sample solution. Different types of building blocks possess negatively charged surfaces characterized with different magnitudes of surface charge. We demonstrate that, by tuning the ionic strength, these distinct surface charges can be utilized to induce assembly of only one selected type of building block in the presence of building blocks of all types. We use virus-like particles (VLPs) derived from the bacteriophage P2238,39 as building blocks. VLPs and other cage-like proteins offer distinct advantages for higher-order assemblies; 12,17,25,27,30,31 these nanostructures are extremely homogeneous in size and can be engineered with additional functionalities via chemical and/or genetic modifications. 13,40,41 The P22 VLP, an icosahedral capsid of a diameter of 56 nm, is a particularly attractive platform due to its versatility in the internal encapsulation of a wide range of functional cargoes including inorganic nanoparticles, 42,43 polymers, 44 and proteins. 45-4 Higher-order assembly of P22 VLPs is governed by the interaction between the exterior surfaces of the VLPs and is independent of the cargoes packaged inside the VLPs. Furthermore, the surface properties of these VLPs, including surface charge, can be easily tuned without altering their overall structure (e.g., shape, size), which enables the study of a higher-order assembly of VLPs in a systematic manner. We previously showed that P22 VLPs self-assemble into ordered

3D arrays, regardless of the cargo encapsulated inside them, when they are mixed with oppositely charged generation 6 (G6) polyamidoamine (PAMAM) dendrimers, which act as linkers. 31 The assembled arrays exhibiting the highest longrange order were formed only near a threshold ionic strength, above which the VLPs did not exhibit any appreciable higherorder assembly. The VLP variants with different surface charges exhibited different ionic strength thresholds.⁴⁸ In the present study, we extend this approach to generate multilayered, ordered protein arrays via the selective, spatially segregated assembly of multiple types of VLP building blocks.

Starting from a mixture of four different types of VLP building blocks produced by tuning the magnitude of the VLP surface charge, the assembly of VLPs of the same type (same surface charge) into spatially segregated regions is directed by modulating the ionic strength of the sample solution in the presence of oppositely charged linkers. The overall structure is defined by a central core, composed of VLPs of a single type, that seeds the formation of multiple layers (shells), each populated with VLPs of only one type. We develop a coarsegrained computational model to describe the selective assembly of a two-component mixture of VLPs into a spatially segregated, ordered core-shell array. The integrated experimental and computational approach enables a clear elucidation of the underlying mechanisms of the self-assembly process responsible for creating these multilayered, ordered materials. The process of assembling such core-shell structures is reversible, and the assembly and disassembly of these arrays is readily controlled through modulating the ionic strength of the solution. The slow and gradual modulation vs a rapid change of the ionic strength also plays an important role in the realization of the core-shell structures. This work establishes a design strategy for synthesizing spatially defined hierarchical architectures that self-assemble from multiple types of nanoscale building blocks in a one-pot fabrication.

RESULTS AND DISCUSSION

Construction of Spatially Segregated Ordered Protein Arrays with Four Distinct Layers. We have demonstrated the construction of hierarchically ordered 3D protein arrays, via the controlled self-assembly of up to four different types of VLP building blocks into layered, core-shell structures (Figure 1a-c). Unlike conventional layer-by-layer assembly strategies in which different layers are added in isolation, 49-51 we assemble the multilayered structure of VLPs from a one-pot mixture containing all types of building blocks. The sequential, type-specific VLP layer formation is mediated by linkers and is controlled by a gradual change in the ionic

strength of the solution (through dialysis), which modulates the electrostatic attraction between VLPs and linkers. We engineered variants of P22 VLP building blocks that exhibit identical morphology but different surface charges (Table 1

Table 1. Peptide Sequence, Zeta Potential at pH 7.0, and the Threshold Ionic Strength of Each P22 VLP Variant

VLP variant	peptide sequence	zeta potential (mV)	threshold ionic strength (I_t) (mM)	I_t estimates from simulation (mM)
P22-EEE2	(VAALEEE) ₂	-43.0 ± 4.1	555	NA
P22-E2	$(VAALEKE)_2$	-30.4 ± 2.8	247	225
P22-Q2	(VAALQSQ) ₂	-23.6 ± 2.0	123	150
P22-K2	$(VAALKEK)_2$	-12.8 ± 2.1	61.7	75

and Figure S2). The surface charge of the VLPs was tuned systematically by introducing two repeats of heptapeptides at the C-terminus of the P22 coat protein, which is exposed on the exterior of the assembled VLP.⁵² Because the P22 VLP is assembled from 420 copies of the coat protein and the C-terminus of the P22 coat protein is exposed outside the VLP, up to 420 copies of these peptides are displayed on the surface. The four different VLP variants, P22-EEE2, P22-E2, P22-Q2, and P22-K2, that possess four different peptides, exhibited negatively charged surfaces with zeta potentials of -43.0, -30.4, -23.6, and -12.8 mV, respectively (Table 1).

In assembly studies involving only a single type of VLP, each of the four variants exhibited a different ionic strength dependence for their self-assembly into higher-order structures when combined with positively charged G6 PAMAM dendrimers of a diameter of 6.7 nm (Figure 1b). The dendrimers acted as bridging linkers connecting the VLPs together through electrostatic interactions. A direct correlation, consistent with our previous study, 48 was found between the zeta potential (surface charge) of a variant and the threshold ionic strength (I_t) , below which VLPs of that variant selfassembled into arrays (and above which no assembly was observed). Specifically, we found the threshold ionic strength values of $I_t^{EE\pm 2} = 555$ mM, $I_t^{E2} = 247$ mM, $I_t^{Q2} = 123$ mM, and $I_t^{K2} = 61.7$ mM for P22-EEE2, P22-E2, P22-Q2, and P22-K2 variants, respectively (Table 1 and Figure 1b). The individual VLP mutants with a higher negative zeta potential exhibited a higher I_t that is, $I_t^{EEE2} > I_t^{E2} > I_t^{Q2} > I_t^{K2}$.

Starting with a mixture of all four types of VLP variants (building blocks) and lowering the ionic strength of the solution via a step-by-step dialysis, VLPs of a specific type assembled into an ordered structure as the ionic strength traversed the associated threshold value I_t . This led to the formation of ordered protein arrays with four distinct layers exhibiting a consistent face-centered cubic (FCC) structure (Figures 1c,d, S3, and S4). Furthermore, this assembly was reversible; when the ionic strength was increased sufficiently above the I_t associated with a particular VLP type, the layer composed of VLPs of that type spontaneously disassembled from the array.

To aid with direct visualization of the layered fabrication, P22-EEE2, P22-E2, P22-Q2, and P22-K2 VLPs were individually labeled with Alexa-488 (green), Texas Red (red), CF405 M (blue), and Alexa-488 fluorescent molecules, respectively (Figures 1a,c, S3, and S4). When equimolar populations of VLPs of these four types were mixed with positively charged G6 PAMAM dendrimers in a solution at

ionic strength I=823 mM (above the threshold values of all the variants), the solution was transparent indicating no assembly of VLPs into arrays. At this high ionic strength (823 mM), the electrostatic attraction between VLPs and G6 dendrimers is highly screened, which suppresses the formation of stable VLP-G6-VLP bridged structures and subsequent assembly of VLPs into 3D arrays.

When the ionic strength of the sample solution was lowered, via dialysis, to I = 494 mM, which is slightly below the I_t of P22-EEE2 ($I < I_t^{EEE2}$) but much greater than the I_t of P22-E2, P22-Q2, and P22-K2 $(I > I_t^{E2} > I_t^{\bar{Q}2} > I_t^{K2})$, the solution became visibly turbid, characteristic of the formation of assembled arrays. Direct observation of the sample using super-resolution fluorescence microscopy revealed the formation of VLP arrays with green color (Figure 1c), signaling that only the P22-EEE2 VLPs assembled into arrays while VLPs of other variants remained as individual particles in the solution. At this ionic strength (494 mM), the electrostatic attraction between VLPs and G6 dendrimers is sufficiently strong to facilitate the formation of VLP-G6-VLP bridged structures for P22-EEE2 VLPs, but too weak to nucleate the bridged structures for any other type of VLP. Upon further lowering of the ionic strength to I = 206 mM, slightly below the I_t of P22-E2 ($I < I_t^{E2}$), fluorescence microscopy images (Figure 1c) showed a redcolored layer (shell) composed of P22-E2 VLPs enveloping the surface of the green-colored P22-EEE2 VLP arrays (core), thus generating a two-layer core-shell array structure. The images also indicated that VLPs of other variant types (Q2 and K2) remained as individual particles in the solution. When the ionic strength of the sample solution was further lowered to I = 103mM, below the I_t of P22-Q2 ($I < I_t^{Q2}$), a blue layer composed of P22-Q2 VLPs was observed enveloping the red-colored P22-E2 VLP layer, generating a three-layer core-shell structure (Figure 1c). Finally, when the ionic strength of the solution was decreased to I = 41 mM, below the threshold of P22-K2 (I $\langle I_t^{K2} \rangle$, the formation of a thin, green layer of P22-K2 VLPs was observed as the fourth, outermost layer (Figures 1c, S3, and S4). Because the surface area of the array increases with an increasing number of shell layers, equimolar amounts of the four building blocks contained in the sample solution yield outermost shell layers that are thinner than the inner core.

Structure Analysis of the Multilayered Protein Arrays with SAXS. Small-angle X-ray scattering (SAXS) measurements of the multicomponent mixture at each of the ionic strength values associated with the dialysis process (823, 494, 206, 103, and 41 mM) verified that the VLPs self-assembled into an ordered FCC structure across the observed multiple layers (Figure 1d). At I = 823 mM, the sample showed a scattering profile that could be ascribed to the form factor of P22 VLPs; no structure factor component was observed, reflecting the dispersed, nonassembly state of all VLPs in the solution. On lowering the ionic strength to I = 494 mM, peaks attributed to the structure factor of an FCC lattice emerged.31,48 These peaks became progressively more prominent as the ionic strength was lowered toward 41 mM. The increase in peak prominence occurs because only the P22-EEE2 VLPs, corresponding to a quarter of the total VLP population, are assembled into an ordered array (core) at I =494 mM, while the form factor arising from the dispersed VLPs of types P22-E2, P22-Q2, and P22-K2 makes a significant contribution to the overall scattering intensity. In stark contrast, when the dialysis experiment reaches I = 41 mM, VLPs of the remaining three types are sequentially assembled

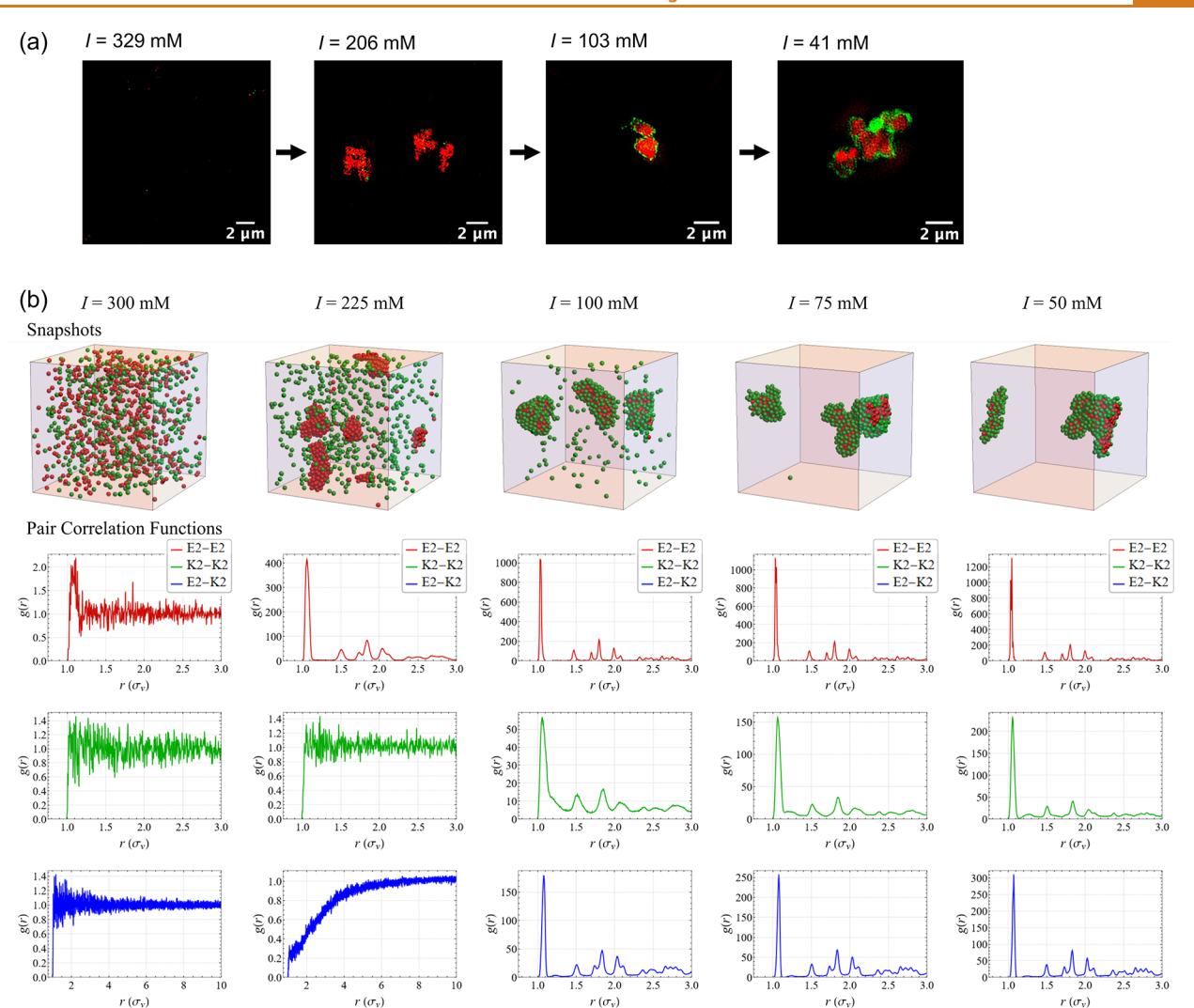


Figure 2. Analysis of the formation of the core-shell structure composed of P22-E2 and P22-K2 VLPs. (a) Super-resolution fluorescence microscope images of the ordered core-shell VLP array formation. When P22-E2 and P22-K2 VLPs were mixed at a 1:1 molar ratio together with an excess of G6 dendrimers at I = 329 mM, the VLPs did not assemble into large aggregates, as the ionic strength is higher than the associated ionic strength thresholds, I_t^{E2} and I_t^{K2} . When the mixture was dialyzed against I = 206 mM, which is lower than I_t^{E2} but higher than I_t^{K2} , only P22-E2 VLPs assembled. At I = 103 mM ($>I_t^{K2}$), a thin layer of P22-K2 VLPs (green) was observed on the surface of the P22-E2 VLP core (red). The shell layer composed of P22-K2 VLPs became thicker when the mixture was dialyzed further to I = 41 mM ($<I_t^{K2}$). (b) Selected simulation snapshots of a typical steady-state configuration of P22-E2 VLPs (red spheres) and P22-K2 VLPs (green spheres) at different ionic strengths indicated by the legend at the top. Ionic strength is decreased from left to right. G6 dendrimers are not shown on the snapshots for clarity. Pair correlation functions (PCFs) of E2-E2 (red, top row), K2-K2 (green, middle row), and E2-K2 (blue, bottom row) VLPs at the corresponding ionic strengths are presented below each snapshot. No assembly is observed at high I = 300 mM (left). Exclusive assembly of P22-E2 VLPs occurs at its threshold ionic strength $I_t^{E2} = 225$ mM $\gg I_t^{K2}$ resulting in an ordered structure (center left); the assembled P22-E2 VLP core actively excludes P22-K2 VLPs as seen in the E2-K2 PCF. Coassembly with a layer of K2 VLPs covering the E2 VLP core occurs upon further dialysis to I = 100 mM (center) and at the K2 threshold, $I_t^{K2} = 75$ mM (center right). Coassembly persists below the ionic strength threshold of P22-K2 variant (right), with PCF peaks sharpening as the ionic strength is reduced to 50 mM.

as layers (shell) into the same ordered structure, leading to a clear enhancement of the structure factor contribution to the overall scattering intensity. The lattice parameter of the FCC array obtained at I = 41 mM was estimated as 86.0 nm from the peak positions (Figure S5). When the sample was dialyzed back from I = 41 mM to higher ionic strength values (up to 823 mM), the peaks attributed to the structure factor gradually diminished, and the form factor became progressively more prominent (Figure 1d). These changes indicate that VLPs of a specific variant progressively disassembled from the ordered array when the ionic strength was increased above the corresponding ionic strength threshold I_t of the variant.

We have previously demonstrated using both experiments and simulations that P22 VLPs of a single type spontaneously self-assemble into an FCC lattice in the presence of G6 dendrimers when the ionic strength of the solution is close to its I_t . At ionic strengths sufficiently lower than I_v VLPs assembled into kinetically trapped amorphous aggregates. ^{31,48} However, we showed that starting from the initial configuration where the VLPs have already assembled into the ordered array near their I_v the ordered FCC structure is sustained even when the ionic strength of the solution is lowered below I_t . ⁴⁸ Thus, the multilayered ordered array, with each layer having assembled near the corresponding I_v

similarly sustains its ordered structure at all ionic strengths below I_t (Figure 1d).

Mechanisms underlying the Formation of Core-shell Arrays: Two-Component VLP Systems. To probe the mechanisms underlying the formation of ordered core-shell protein arrays in detail, we investigated the two-component (binary) system containing VLPs of two types, P22-E2 and P22-K2, using experiments and molecular dynamics (MD) simulations. As expected, a two-layer core-shell structure composed of spatially segregated P22-E2 (red) and P22-K2 (green) VLPs was observed in experiments by decreasing the ionic strength from I = 329 to 41 mM via a step-by-step dialysis (Figures 2a and S6). According to the estimation of the yield of the arrays, nearly 97% of the P22 VLPs in the starting solution were assembled into arrays (Supporting Information Section 1). A preliminary analysis of the long-term stability of the assembled structures was conducted by storing the twocomponent core-shell array sample at 4°C for 17 months after preparation and observing it with super-resolution fluorescence microscopy. Over this time frame, the core-shell architecture was maintained, and some arrays coalesced (Figure S7).

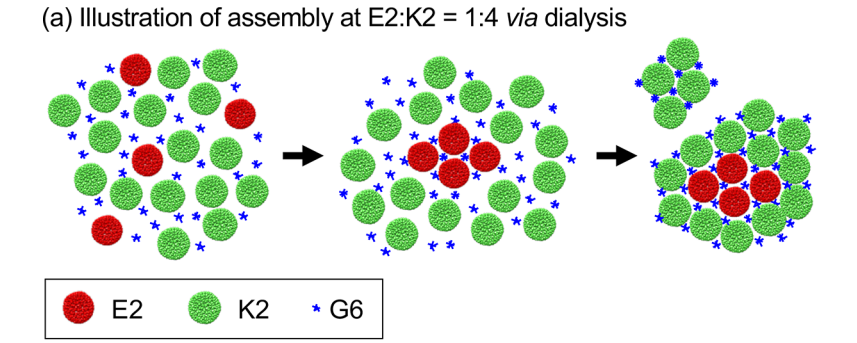
The two-component VLP system was investigated via MD simulations using a coarse-grained model adapted from our previous study describing the linker-mediated assembly of single-component VLP systems characterized with VLPs of only one variant. 48 P22-E2 and P22-K2 VLPs were modeled as 56 nm wide charged spheres with charges of -1500e and -600e, respectively. G6 dendrimers were modeled as positively charged spheres of a diameter of 6.7 nm. The steric interactions between a pair of VLPs and between a pair of dendrimers were modeled using the standard purely repulsive Lennard-Jones (LJ) potential. To account for the significant differences in the sizes of the VLPs and the dendrimers, the VLP-dendrimer steric interactions were modeled using a modified LJ potential characterized by a parameter σ_{hc} , which controls the degree of proximity of dendrimers to the VLP surface (see Methods). The VLP-VLP, VLP-dendrimer, and dendrimer-dendrimer electrostatic interactions were modeled using the standard Yukawa potential. This model system was the same as the one developed in our previous study, 48 except for the reparametrization of the dendrimer charge and $\sigma_{h\phi}$ which was informed by experimental studies of the assembly of highly charged single-component VLP systems (e.g., P22-EEE2). Specifically, the dendrimer charge was increased to 45e, and the VLP-dendrimer steric repulsion was altered by choosing σ_{hc} = 4.5 nm. These modifications enabled an appropriate dependence of VLP assembly on ionic strength for the highly charged VLP variants, yet preserved the assembly behavior found in our previous paper for the single-component VLP systems (P22-E2, P22-Q2, P22-K2). Further, the reparameterized coarse-grained model enabled the study of the two-component system with both rapid and gradual changes in the ionic strength of the solution. All simulations were performed in an NVT ensemble at a temperature of 298 K. The Methods section provides more details about the model parameters, interaction potentials, and simulation protocols.

In simulating dialysis, ionic strength values were updated in a stepwise fashion, allowing for the equilibration of the system between each step. This coarse-grained model successfully reproduced the binary core-shell array formation composed of two equimolar populations of VLPs corresponding to P22-E2 and P22-K2 variants (Figures 2b and Figure S8). Previous

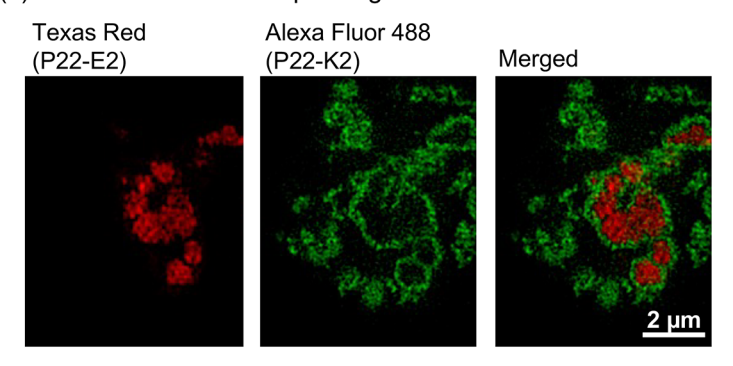
work showed that P22-E2 VLPs assemble into ordered arrays at an ionic strength threshold $I_t^{E2} \approx 225$ mM, while P22-K2 VLPs only assemble when a much lower ionic strength threshold $I_t^{K2} \approx 75$ mM is reached (note the small differences in the threshold values associated with simulations and experiments (Table 1); simulation estimates are within 25 mM of the experimental results). Because of this disparity in ionic strength thresholds and the gradual nature of dialysis, it is possible to selectively establish the electrostatic drive to assemble P22-E2 VLPs in a mixed system of P22-E2 and P22-K2 VLPs. Gradually decreasing the ionic strength from nonassembly conditions to I_t^{E2} leads to an assembly of only P22-E2 VLPs into an ordered array (core), as illustrated in the simulation snapshots (Figure 2b). Further lowering of I to $I \approx$ I_t^{K2} yields coassembly into core-shell structures with a layer of P22-K2 VLPs enveloping the core formed by P22-E2 VLPs. Simulations also confirmed the ionic-strength-dependent reversible nature of the core-shell assembly and disassembly (Figure S9).

The pair correlation functions (PCFs) associated with P22-E2 VLPs (E2-E2 PCF), P22-K2 VLPs (K2-K2 PCF), and P22-E2 and P22-K2 (E2-K2 cross-PCF) VLPs quantitatively illustrate the electrostatic control mechanism for realizing core-shell structures via the dialysis-based modulation of ionic strength (Figure 2b). Above the ionic strength threshold of either species, there is little more than a transient first peak characterizing a nonassembly configuration. This is the product of fleeting, weak interactions at short distances between VLPs. During the initial exclusive assembly of the higher-charged species (P22-E2 VLPs) at $I_t^{E2} \approx 225$ mM, the correlations in the entire system are dominated by those associated with P22-E2 VLPs (E2-E2 correlations). The corresponding PCF (red in Figure 2b) exhibits an ordered HCP/FCC lattice structure, similar to that observed in our earlier work.⁴⁸ This structure provides the core for the core-shell structures resulting from subsequent dialysis. At an ionic strength $I_t^{E2} \approx 225$ mM, the K2-K2 PCF (green in Figure 2b) shows no significant assembly of P22-K2 VLPs, consistent with the ionic strength threshold for the K2 variant. Further, the E2-K2 cross-PCF (blue in Figure 2b) at $I_t^{E2} \approx 225$ mM shows the exclusion of P22-K2 VLPs from the P22-E2 VLP core as evident from the smaller than 1 PCF values until a distance greater than 7 VLP diameters, a rough approximation of the size of the P22-E2 VLP core array, considering finite-size effects in simulations.

Interestingly, simulation snapshots and the PCFs indicate that upon further dialysis, P22-K2 VLPs start forming a layer (shell) surrounding the P22-E2 VLP core at an ionic strength above the threshold ionic strength $I_t^{K2} \approx 75$ mM for assembly of the single-component P22-K2 VLP system (Figure 2b). Even at I = 100 mM $(I > I_t^{K2})$, clear and defined peaks in the K2-K2 PCF are observed, indicating a significant population of P22-K2 VLPs in the solution have already started to form the layer (shell) on the surface of the P22-E2 VLP core (see Figure S8 for a cross section of this core-shell array). The population of the P22-K2 VLPs in this layer increases further as the ionic strength is lowered to I = 75 mM. We posit a scenario based on the accumulation of dendrimers (linkers) on the surface of the already formed core to explain this finding. In our previous study, simulations of the single-component P22-E2 VLP system showed a significant rise in the average number of dendrimers (linkers) condensed on the surface of the P22-E2 VLPs at low ionic strengths. 48 This effect was also observed to persist in the assembly of the two-component system, as



(b) Fluorescence microscope images



(c) Simulations of assembly at E2:K2 = 1:4

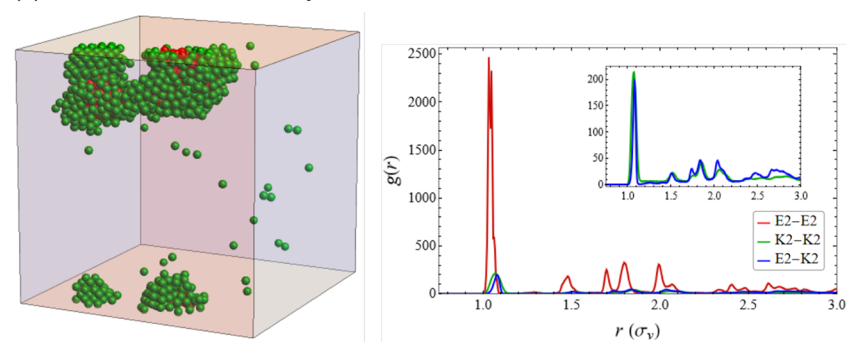


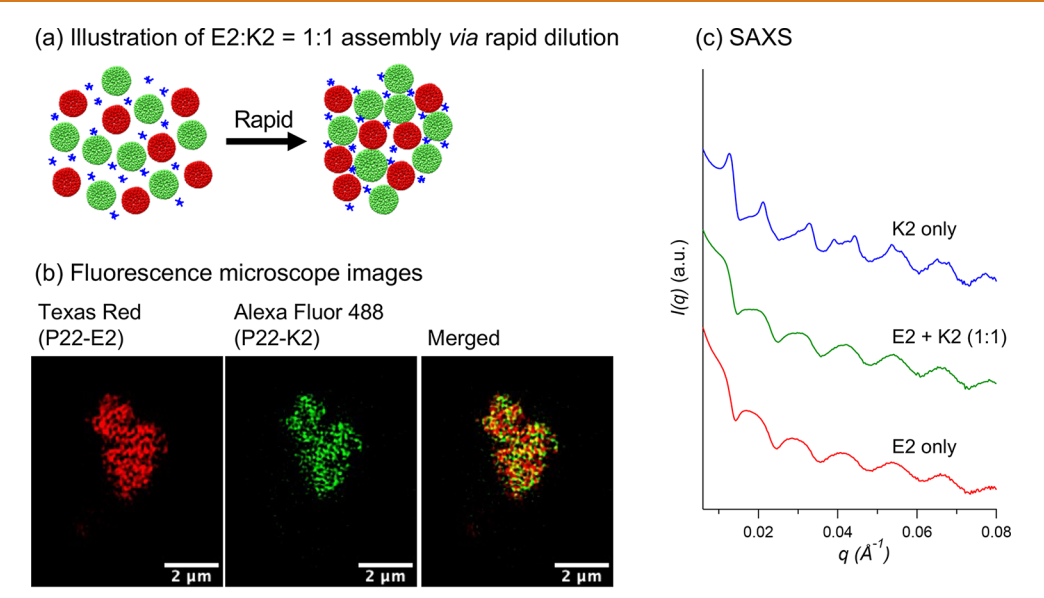
Figure 3. Assembly of P22-E2 and P22-K2 VLPs with a 1:4 stoichiometry ratio via dialysis. (a) Schematic showing assembly of P22-E2 and P22-K2 VLPs. For an E2:K2 = 1:4 stoichiometric ratio, formation of core-shell structures persists, yet homogeneous nucleation and growth of K2-only assembly becomes more prominent. (b) Fluorescence microscopy observations of a sample showed that in addition to the E2-K2 core-shell assembly, a standalone K2-only array formation also readily occurred when the sample was dialyzed from the ionic strength I = 329 to 41 mM via 206 mM. (c) Simulation snapshot (left) and associated PCFs (right) for a dialyzed sample are shown. In the PCFs, red, green, and blue profiles denote E2-E2, K2-K2, and E2-K2 VLP correlations, respectively. The PCFs are shown at the ionic strength threshold of the lower charged species (75 mM). Inset shows K2-K2 and E2-K2 correlations with zooming in on the y-axis of the outset. The coreshell assembly is seen to persist, wherein peak positions in the PCF remain similar to those observed in the E2:K2 = 1:1 case (Figure 2b).

evidenced by the dramatic rise in the average number of dendrimers per VLP (Figures S11 and S12). We hypothesize that this enhanced local linker concentration on the surface of the P22-E2 VLP core increases the potential for P22-K2 VLPs to bind to the P22-E2 VLPs associated with the core at an ionic strength higher than the threshold ionic strength I_t^{K2} (~75 mM) based on the isolated assembly of the P22-K2 VLP system.

The P22-K2 VLP layer (shell) formation at an ionic strength higher than I_t^{K2} was experimentally verified (I = 103 mM in Figure 2a). Consistent with simulations, a thin layer of P22-K2 VLPs (green) formed on the surface of the already-formed array composed of P22-E2 VLPs (red) when the ionic strength

was lowered to I=103 mM, which is higher than $I_t^{\rm K2}$. It should be noted that the P22-K2 VLPs alone with G6 dendrimers did not assemble into an array at I=103 mM (Figure S10). The simulation and experimental results suggest that the accumulation of the dendrimers on the surface of the P22-E2 VLP core makes the core surface a unique recruiting site for P22-K2 VLPs, leading to the formation of a thin layer of P22-K2 VLPs even at an ionic strength higher than $I_t^{\rm K2}$. These findings show a clear preference in a two-component system toward the formation of the binary core-shell arrays over isolated cores of only P22-K2 VLPs at the lowest ionic strengths. In addition, when the ionic strength was lowered to I=41 mM, the thickness of the shell composed of P22-K2 VLPs was observed

ACS Nano www.acsnano.org Article





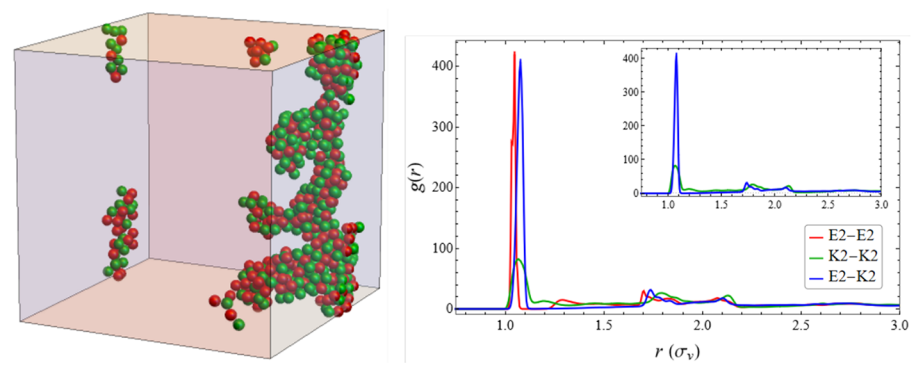


Figure 4. Assembly of P22-E2 and P22-K2 VLPs into arrays via a rapid change of the ionic strength from I=329 to 41 mM. (a) Rapid dilution leads to a homogeneous distribution of VLPs in an amorphous aggregate. (b) Fluorescence microscopy images indicate that, unlike the slow dialysis process, E2 and K2 VLPs distributed homogeneously in the aggregates. (c) SAXS profiles of P22 VLP arrays assembled via rapid dilution of the ionic strength from I=329 mM to 41 mM. The E2-K2 binary sample as well as the E2-only sample do not exhibit a structure factor in the SAXS profiles, which is characteristic of amorphous aggregates. In contrast, the K2-only sample has a prominent structure factor attributed to an ordered FCC arrangement. (d) Simulation snapshot (left) and PCFs (right) for the rapid change in ionic strength from I=329 to 75 mM are shown. Inset shows K2-K2 and E2-K2 correlations with zooming in on the y-axis of the outset. In the case of gradual change via dialysis shown in Figure 2b, a clear core is formed at high ionic strengths, which—due to the disparate time scales of dialysis and assembly—is followed by layered deposition of the lower-charged species. Rapid dilution circumvents this time scale disparity and does not allow for the P22-E2 core formation prior to the P22-K2 VLP shell deposition. Instead, a homogeneous mixing of the P22-E2 VLPs (red spheres) and P22-K2 VLPs (green spheres) is observed at I=75 mM. PCFs similarly suggest that rapid dilution leads to kinetically trapped, amorphous aggregates at this low ionic strength.

to increase (I=41 mM in Figure 2a), indicating that additional P22-K2 VLPs incorporated into the shell layer near I_t^{K2} . A considerable increase in the K2-K2 PCF peak heights and the lack of isolated K2 VLPs at 75 and 41 mM (compared to 100 mM) in the snapshots (Figure 2b) also suggested that more K2 VLPs were recruited on the surface of the E2 VLP core as the ionic strength was lowered to values near I_t^{K2} .

Dialyzing gradually to the ionic strength threshold of the lower-charged variant ($I_t^{K2} \approx 75$ mM) and below sharpens the peaks associated with all PCFs, in particular the K2-K2 PCF (Figure 2b). While structure analysis with SAXS indicates that the entire core-shell VLP array structure exhibits order consistent with an FCC lattice, it is experimentally difficult to isolate the contributions to the order in terms of the emergence of lattice structure within each layer and across the

interface of the two layers (i.e., epitaxy growth of the second layer on the surface of the first layer). In simulations, the E2-K2 cross-correlation PCFs show peaks at positions corresponding to those associated with both E2-E2 (core) and K2-K2 (shell) correlations, which is indicative of the presence of the same FCC lattice characterizing the ordered array with P22-K2 VLPs acting as a shell extension of the P22-E2 VLP core. Furthermore, a clear sharpening of the PCF peaks associated with E2-E2, K2-K2, and E2-K2 correlations as dialysis proceeds below the threshold of both species to $I=50~\rm mM$ indicates that the enhancement in the order of the array structure arises due to the VLPs present within each layer and the VLPs associated with the E2-K2 interface. We also note that the SAXS profiles obtained in experiments and the PCFs of ordered VLP arrays extracted from simulations indicate that

the lattice of the VLP array contracted slightly when the ionic strength was lowered (Figure S13). The contraction can be attributed to the stronger electrostatic interactions between negatively charged VLPs and positively charged dendrimers due to a longer Debye screening length at lower ionic strength. Both sharpening of the peaks and contraction of the lattice align with intuition: stronger electrostatic forces counteract thermodynamic fluctuations away from a close-packed ground state.

The assembly of different species of VLPs controlled by modulating ionic strength implies that changes in their relative abundance (i.e., their stoichiometric ratios) might also influence the fabrication of core-shell structures. The molar ratio of E2:K2 in the samples shown in Figure 2 was 1:1. When the molar ratio of these two building blocks was changed to 1:4, two different types of structures were readily observed (both experimentally and computationally): arrays with a consistent core-shell structure and arrays composed of only P22-K2 VLPs (Figure 3). This coexistence suggests that the homogeneous, isolated assembly of P22-K2 VLPs becomes progressively more favorable as the relative proportion of P22-K2 VLPs is increased.

A gradual change of ionic strength in the solution is critical for the fabrication of well-ordered core-shell structures. When the ionic strength of a solution containing P22-E2 VLPs, P22-K2 VLPs, and dendrimers was reduced rapidly from 329 to 41 mM, the two types of VLPs did not assemble into a core-shell array with an ordered arrangement but rather formed an amorphous aggregate in which the two types of VLPs were homogeneously distributed (Figure 4). Unlike slow modulation of the ionic strength via dialysis, rapidly assembling systems—formed by the quick reduction of ionic strength wellbelow that of the ionic strength threshold for the P22-E2 variant—yield kinetically trapped, amorphous P22-E2 VLP aggregates (Figure 4c, bottom), which resembles glass formation by rapid quenching. On the other hand, the P22-K2 VLP only system yielded an ordered array (Figure 4c, top) despite the rapid dilution, because the ionic strength of 41 mM is close to its threshold ionic strength ($I_t^{K2} = 61.7$ mM). The amorphous aggregate formation was observed in the binary system of P22-E2 and P22-K2 VLPs in experiments (Figure 4a-c, middle) and in simulations (Figure 4d), suggesting that the kinetic trapping of P22-E2 VLPs disrupts the arrangement of P22-K2 VLPs in what would otherwise be the assembly of P22-K2 VLPs into well-ordered arrays at the associated threshold ionic strength I_t^{K2} .

CONCLUSION

Spatially defined hierarchical organization of cells and biomolecules is one of the defining features of biological systems. While scientists have drawn inspiration for materials design from biological structures, controlling the spatial arrangement of multiple types of building blocks into hierarchically organized structures is still a synthetic challenge. Here, we have demonstrated a self-assembly-based approach of fabricating spatially segregated core-shell architectures from multiple types of VLPs whose surface charges were finely tuned. Importantly, this fabrication was achieved in a one-pot synthesis by modulating the ionic strength through a dialysis process. Gradual modulation of ionic strength was critical to develop an ordered core-shell structure rather than a kinetically trapped, amorphous structure.

We also developed a coarse-grained computational model, which successfully predicted the experimentally observed coreshell array formation for the two-component system, providing insights into the mechanism of the spatially segregated assembly of multiple types of VLPs. For example, formation of the P22-K2 VLP layer on the P22-E2 VLP core at an ionic strength higher than the ionic strength threshold for the P22-K2 variant was predicted via simulations prior to the experimental assessment. Similar integrated experimental-computational approaches will be valuable in exploring the regions of the material design space exhibiting the formation of bioinspired macromolecular assemblies such as the multi-layered, ordered arrays reported in this work.

VLPs encapsulating a wide range of functional cargoes such as enzymes and inorganic nanoparticles have been prepared by many research groups. 13,54,55 The approach to fabricate hierarchically organized and spatially segregated arrays presented in this study can be readily applied to control the arrangement of a diverse population of VLP building blocks with various functionalities. This facilitates the design of ordered array materials with emerging functionality arising from the interaction between the individual building blocks, including the ability to control core-shell layering vs homogeneous clustering of VLPs with different cargoes in order to desirably tune cargo reactivity and catalysis.

METHODS

ı

Methods for preparation and characterization of P22 VLP mutants and labeling of P22 VLPs with fluorescent molecules are provided in the Supporting Information.

Construction of Multilayered Ordered VLP Arrays. The ability to construct multilayered core-shell VLP arrays was investigated using stepwise modulation of ionic strength via dialysis. To construct four-layered core-shell arrays, four types of P22 VLPs, i.e., P22-EEE2, P22-E2, P22-Q2, and P22-K2, were used as building blocks. Concentration of each VLP was adjusted to 50 nM in a sodium phosphate buffer with I = 823 mM (sodium phosphate 200 mM, sodium chloride 400 mM, pH 7.0). The PAMAM G6 dendrimer was diluted in the same buffer solution at a ratio of 1:4 (v/v). Equivalent molar amounts of each type of VLP were mixed unless otherwise stated followed by addition of the G6 dendrimer at a defined ratio of 1000-fold excess of dendrimer per VLP. The mixed solution was then transferred into a 12-14 kDa molecular weight cutoff dialysis tubing (Spectra/Por 4) and sequentially dialyzed against buffers with I = 494, 329, 206, 103, and 41 mM for 3 h each. The sample reached at the lowest ionic strength was dialyzed back to higher-ionic-strength buffers to examine reversible disassembly of the arravs.

To prepare two-layered core-shell arrays, P22-E2 and P22-K2 VLPs in $I=329~\mathrm{mM}$ were used as the building blocks. After mixing with G6 dendrimers, the sample solution was dialyzed in a stepwise manner similar to the preparation of the four-layered arrays. Some VLP array samples were prepared via rapidly lowering the ionic strength (within a few seconds) instead of stepwise slow modulation via dialysis. For these samples, solutions of $I=329~\mathrm{mM}$ containing P22-E2 and/or P22-K2 VLPs with G6 dendrimers were diluted with ultrapure water in order to drop the ionic strength to 41 mM. Water was added quickly to the sample solution with a pipet while stirring. The sample solution immediately turned cloudy.

Super-resolution 3D-Structured Illumination Microscopy (SIM). Core-shell arrays of VLPs constructed from the fluorescently labeled P22 VLPs at various ionic strengths were imaged using the DeltaVision OMX-SR 3D-SIM (Cytiva) equipped with a 1.42 NA Olympus 60× oil objective. The array samples were diluted with a buffer at the corresponding ionic strength. After a SecureSeal imaging spacer (13 mm inner diameter × 0.12 mm thickness, Grace Bio-Laboratories) was attached on a no. 1.5 microcover glass (22 × 22

mm), 20 μ L of each sample was spotted on the cover glass just before imaging. A microscope slide (25 × 75 mm) was gently placed on the cover glass with the spacer to seal the sample. Immersion oil with a reflective index of 1.516 was used when the sample cover glass was mounted on the microscope. Laser lines of 405 nm with emission filters of 419–465 nm, 488 nm with emission filters of 500–550 nm, and 561 nm with emission filters of 609–654 nm were used for collecting CF 405M, Alexa Fluor 488, and Texas Red signals, respectively. The z-axis section spacing was 0.125 μ m. Fluorescent images of the VLP arrays were acquired using DeltaVision-OMX image acquisition software, while the images were reconstructed using softWoRx image processing software. Collected fluorescent images were processed in terms of brightness and contrast using ImageJ software (version 2.1.0/1.53c).

Small-Angle X-ray Scattering (SAXS) Measurements. SAXS measurements were carried out at the 12-ID-B beamline at the Advanced Photon Source (APS). The measurements were conducted at 13.3 keV, and the scattering data were collected using a Pilatus 2 M detector. A volume of 100 μ L of each sample was injected and continuously agitated by a syringe pump during the measurement to minimize radiation damage and prevent sedimentation. The scattering angle was calibrated using silver behenate as a standard. A total of 20 scattering patterns were collected from each sample and averaged, while each scattering pattern was acquired for 1 s with 2 s intervals. One-dimensional scattering profiles were obtained by averaging two-dimensional scattering patterns. The data were presented as scattering intensity as a function of scattering vector, q

$$q = \frac{4\pi}{\lambda} \sin \theta \tag{1}$$

where θ is half of the scattering angle 2θ and λ is the X-ray wavelength used for the measurements.

Coarse-Grained Model and Simulation Details. The electrostatic interactions between each pair (i,j) of spherical particles separated by a (center-to-center) distance $r_{ij} = r$ are modeled using the standard Yukawa potential

$$u_{E}(r) = q_{i}q_{j} \frac{e^{\kappa(\frac{\sigma_{i}+\sigma_{j}}{2})}}{\left(1 + \kappa(\frac{\sigma_{i}}{2})\right)\left(1 + \kappa(\frac{\sigma_{j}}{2})\right)} (l_{B}e^{-\kappa r})$$
(2)

where u_E is measured in units of k_BT and q_i is the net surface charge associated with the ith particle measured in units of the electronic charge e. $l_{B}=\frac{e^{2}}{(4\pi\epsilon_{0}\epsilon_{w}k_{B}T)}\approx$ 0.7 nm is the Bjerrum length in water at temperature T=298 K, where ϵ_0 is the permittivity of the vacuum and $\epsilon_w = 78.5$ is the dielectric constant of water. $\kappa = \lambda_D^{-1} = \sqrt{8\pi l_B I}$ is the inverse of the Debye screening length λ_D , where $I = \frac{1}{2} \sum_{i=1}^n c_i z_i^2$ is the ionic strength of the solution characterized by electrolyte ions of concentration c_i with valence z_i . Ionic strength, I, was swept from 10 to 300 mM changing λ_D from 3.04 to 0.514 nm. All simulations were performed at a VLP concentration of $c_v = 370$ nM (10 times greater than the experimental value) and dendrimer concentration of 37 μ M (the same bulk concentration as in experiments). Most properties of the assembly of single-component systems at $c_v = 370$ nM, including the ionic strength threshold to assemble into ordered structures, were consistent with the assembly behavior observed in our previous study involving simulations at experimental concentrations (VLPs at 37 nM and dendrimers at 37 μ M). In simulating dialysis, ionic strength and associated κ values are updated in a stepwise fashion, allowing for equilibration between each step. The entire system is first equilibrated at 300 mM, after which the ionic strength is decreased to 225 mM. After equilibration at 225 mM, the ionic strength is reduced in steps of 25 mM down to 50 mM (that is, VLP systems are sequentially transitioned to and equilibrated at 200, 175, 150, 125, 100, 75, and 50 mM). In the case of rapid dilution, the system is prepared at a high ionic strength of 300 mM, and the ionic strength is quickly reduced (in one step) to the target low ionic strength (e.g., 75 mM).

P22 VLPs of all types and dendrimers are modeled as smooth spheres of diameter $\sigma_v = 56$ nm and diameter $\sigma_d = 6.7$ nm, respectively. The steric interactions between a pair of VLPs and between a pair of dendrimers are modeled using the standard purely repulsive Lennard-Jones potential

$$u_{LJ}(r) = 1 + 4\left(\left(\frac{\sigma}{r}\right)^{12} - \left(\frac{\sigma}{r}\right)^{6}\right) \tag{3}$$

for $r \leq \sqrt[6]{2} \, \sigma$, where u_{IJ} is measured in units of k_BT and σ is the particle diameter. For $r \geq \sqrt[6]{2} \, \sigma$, $u_{LJ}(r) = 0$. The steric interactions between a VLP and a dendrimer are modeled using the modified Lennard-Jones potential to account for significant differences in the size of the particles

$$u_{mLJ}(r) = 1 + 4 \left(\left(\frac{\sigma_{hc}}{r - \Delta_{ij}} \right)^{12} - \left(\frac{\sigma_{hc}}{r - \Delta_{ij}} \right)^{6} \right)$$

$$\tag{4}$$

for $\Delta_{ij} < r < \sqrt[6]{2} \, \sigma_{hc} + \Delta_{ij}$, where u_{mLJ} is measured in units of $k_B T$ and $\Delta_{ij} = (\sigma_v + \sigma_d)/2 - \sigma_{hc}$. For $r \le \Delta_{ij}$, $u_{mLJ}(r) = \infty$, and for $r \ge \sqrt[6]{2} \, \sigma_{hc} + \Delta_{ij}$, $u_{mLJ}(r) = 0$. The σ_{hc} parameter effectively accounts for the degree of proximity of dendrimers to the VLP surface and tunes the average distance of closest approach between a dendrimer and a VLP.

This model system is the same as the one developed in our previous study;⁴⁸ however, a few model parameters are updated, informed by experimental studies of a higher-order assembly of highly charged single-component VLP systems (e.g., P22-EEE2). The modifications enabled an appropriate dependence of the VLP assembly on ionic strength for these highly charged VLP variants yet preserved the assembly behavior found in our previous paper for the single-component VLP systems (P22-E2, P22-Q2, P22-K2). Specifically, dendrimer charge was increased to q_d = 45e (from q_d = 35e), and the VLP-dendrimer steric repulsion was altered by choosing a smaller σ_{hc} = 4.5 nm (from σ_{hc} = 6.7 nm), which corresponded to a distance of ~31 nm for the VLP-dendrimer closest approach distance, ~0.3 nm smaller than the VLP-dendrimer touching distance. These updates result in minimal changes to the behavior of the model as it pertains to the single-VLP-type systems. At the same virus and dendrimer concentrations as before, the thresholds I_t increase minimally: K2 VLPs now assemble at $I_t^{K2} = 75$ mM (up from 58 mM), and the E2 threshold is increased slightly.

Pair correlation functions (PCF) between VLPs are used for characterizing the order of the assembly. The self-PCF g(r) characterizing the correlations between VLPs of the same type (e.g., P22-E2 VLPs) is computed following the standard procedure adopted in our previous paper. As is similar process, briefly described next, is employed for computing the cross-PCF $g_{IJ}(r)$ characterizing the correlations between VLPs of different types (e.g., between P22-E2 and P22-K2 VLPs). Consider N_I particles of type I and N_J particles of type I. $g_{IJ}(r)$ represents the average relative density of IJ pairs separated by a distance r in a sample of volume V and is calculated as the average density of particles of type I at a distance r from particles of type I normalized by the expected number density at that distance for an ideal gas. $g_{IJ}(r)$ is given by

$$g_{IJ}(r) = \frac{V < \sum_{i=1}^{N_I} \sum_{j=1}^{N_J} \delta(r - r_{ij}) >}{N_I N_I}$$
(5)

where $\delta(r-r_{ij})$ is the Dirac-delta function, r_{ij} is the distance between the i^{th} particle of type I and the j^{th} particle of type I, and <> denotes an ensemble average performed over trajectory samples collected during a selected time window. The delta function represents the density of IJ pairs separated by a distance r. In practice, we consider the position of a particle of type I as a reference center and count the number of particles of type I surrounding the central particle within a spherical shell of radius r and thickness dr. This count is divided by

the spherical shell volume. Note that the cross-correlative PCF is symmetric with respect to particle types, that is, $g_{IJ}(r) = g_{II}(r)$.

ASSOCIATED CONTENT

Supporting Information

The Supporting Information is available free of charge at https://pubs.acs.org/doi/10.1021/acsnano.1c11272.

DNA sequences of protein building blocks, additional experimental details, and additional results (PDF)

AUTHOR INFORMATION

Corresponding Authors

Trevor Douglas — Department of Chemistry, Indiana University, Bloomington, Indiana 47405, United States; orcid.org/0000-0002-7882-2704; Phone: (812) 856-6936; Email: trevdoug@iu.edu; Fax: (812) 856-5710 Vikram Jadhao — Intelligent Systems Engineering, Indiana University, Bloomington, Indiana 47408, United States; orcid.org/0000-0002-8034-2654; Phone: (812) 856-4018; Email: vjadhao@iu.edu

Authors

Masaki Uchida – Department of Chemistry and Biochemistry, California State University, Fresno, Fresno, California 93740, United States; Department of Chemistry, Indiana University, Bloomington, Indiana 47405, United States; ⊚ orcid.org/ 0000-0003-0710-8834

Nicholas E. Brunk — Intelligent Systems Engineering, Indiana University, Bloomington, Indiana 47408, United States; Wolfram Research, Champaign, Illinois 61820, United States; VeriSIM Life Inc., San Francisco, California 94104, United States; orcid.org/0000-0001-5444-799X

Nathasha D. Hewagama — Department of Chemistry, Indiana University, Bloomington, Indiana 47405, United States

Byeongdu Lee — X-ray Science Division, Advanced Photon Source, Argonne National Laboratory, Argonne, Illinois 60439, United States; orcid.org/0000-0003-2514-8805

Peter E. Prevelige, Jr. – Department of Microbiology, University of Alabama at Birmingham, Birmingham, Alabama 35294, United States

Complete contact information is available at: https://pubs.acs.org/10.1021/acsnano.1c11272

Author Contributions

[#]M.U. and N.E.B. contributed equally to this work.

Notes

The authors declare no competing financial interest.

ACKNOWLEDGMENTS

This work was supported by the National Science Foundation grants CMMI-1922883, DMR-1753182, and 1720625. We thank the IU Light Microscopy Imaging Center (LMIC), the Electron Microscopy Center, the Nanoscale Characterization Facility, and the Laboratory for Biological Mass Spectrometry for access to their instrumentation. The OMX-SR microscope at the LMIC was acquired under the National Institutes of Health (NIH) award NIH1-S10OD024988-01. We also thank Dr. J. Powers of the LMIC for help and advice. This research used resources of the Advanced Photon Source, a U.S. Department of Energy (DOE) Office of Science user facility at Argonne National Laboratory and is based on research

supported by the U.S. DOE Office of Science-Basic Energy Sciences, under Contract No. DE-AC02-06CH11357.

REFERENCES

- (1) Steinberg, M. S. Differential Adhesion in Morphogenesis: A Modern View. Curr. Opin Genet Dev 2007, 17, 281–286.
- (2) Townes, P. L.; Holtfreter, J. Directed Movements and Selective Adhesion of Embryonic Amphiblian Cells. *J. Exp Zoolog A: Comp Exp Biol.* **1955**, *128*, 53–120.
- (3) Foty, R. A.; Steinberg, M. S. The Differential Adhesion Hypothesis: A Direct Evaluation. *Dev. Biol.* **2005**, 278, 255–263.
- (4) Tao, K.; Makam, P.; Aizen, R.; Gazit, E. Self-Assembling Peptide Semiconductors. *Science* **2017**, *358*, aam9756.
- (5) Kuzyk, A.; Schreiber, R.; Fan, Z.; Pardatscher, G.; Roller, E. M.; Hogele, A.; Simmel, F. C.; Govorov, A. O.; Liedl, T. DNA-Based Self-Assembly of Chiral Plasmonic Nanostructures with Tailored Optical Response. *Nature* **2012**, *483*, 311–314.
- (6) Xiong, H.; Sfeir, M. Y.; Gang, O. Assembly, Structure and Optical Response of Three-Dimensional Dynamically Tunable Multicomponent Superlattices. *Nano Lett.* **2010**, *10*, 4456–4462.
- (7) Shevchenko, E. V.; Talapin, D. V.; Kotov, N. A.; O'Brien, S.; Murray, C. B. Structural Diversity in Binary Nanoparticle Superlattices. *Nature* **2006**, 439, 55–59.
- (8) Nykypanchuk, D.; Maye, M. M.; van der Lelie, D.; Gang, O. DNA-Guided Crystallization of Colloidal Nanoparticles. *Nature* **2008**, 451, 549–552.
- (9) Macfarlane, R. J.; Lee, B.; Jones, M. R.; Harris, N.; Schatz, G. C.; Mirkin, C. A. Nanoparticle Superlattice Engineering with DNA. *Science* **2011**, 334, 204–208.
- (10) Laramy, C. R.; O'Brien, M. N.; Mirkin, C. A. Crystal Engineering with DNA. *Nature Reviews Materials* **2019**, *4*, 201–224.
- (11) McMillan, J. R.; Hayes, O. G.; Winegar, P. H.; Mirkin, C. A. Protein Materials Engineering with DNA. *Acc. Chem. Res.* **2019**, *52*, 1939–1948.
- (12) Korpi, A.; Anaya-Plaza, E.; Valimaki, S.; Kostiainen, M. Highly Ordered Protein Cage Assemblies: A Toolkit for New Materials. WIREs Nanomed Nanobiotechnol 2020, 12, No. e1578.
- (13) Aumiller, W. M.; Uchida, M.; Douglas, T. Protein Cage Assembly across Multiple Length Scales. *Chem. Soc. Rev.* **2018**, 47, 3433–3469.
- (14) Matsuurua, K. Rational Design of Self-Assembled Proteins and Peptides for Nano- and Micro-Sized Architectures. RSC Adv. 2014, 4, 2942–2953.
- (15) Ueno, T. Porous Protein Crystals as Reaction Vessels. Chem. Eur. J. 2013, 19, 9096–9102.
- (16) Wei, H.; Wang, Z.; Zhang, J.; House, S.; Gao, Y. G.; Yang, L.; Robinson, H.; Tan, L. H.; Xing, H.; Hou, C.; et al. Time-Dependent, Protein-Directed Growth of Gold Nanoparticles within a Single Crystal of Lysozyme. *Nat. Nanotechnol* **2011**, *6*, 93–97.
- (17) Zhang, L.; Bailey, J. B.; Subramanian, R. H.; Groisman, A.; Tezcan, F. A. Hyperexpandable, Self-Healing Macromolecular Crystals with Integrated Polymer Networks. *Nature* **2018**, *557*, 86–91.
- (18) Zhang, Y.; Zhang, X.; Tang, J.; Snow, C. D.; Sun, G.; Kowalski, A. E.; Hartje, L. F.; Zhao, N.; Wang, Y.; Belfiore, L. A. Synthesis of Luminescent Lanthanide Complexes within Crosslinked Protein Crystal Matrices. *CrystEngComm* **2018**, *20*, 2267–2277.
- (19) Lopez, S.; Rondot, L.; Lepretre, C.; Marchi-Delapierre, C.; Menage, S.; Cavazza, C. Cross-Linked Artificial Enzyme Crystals as Heterogeneous Catalysts for Oxidation Reactions. *J. Am. Chem. Soc.* **2017**, *139*, 17994–18002.
- (20) Abe, S.; Pham, T. T.; Negishi, H.; Yamashita, K.; Hirata, K.; Ueno, T. Design of in-Cell Protein Crystal for Environmentally Responsive Construction of a Supramolecular Filament. *Angew. Chem., Int. Ed. Engl.* **2021**, *60*, 12341.
- (21) Suzuki, Y.; Cardone, G.; Restrepo, D.; Zavattieri, P. D.; Baker, T. S.; Tezcan, F. A. Self-Assembly of Coherently Dynamic, Auxetic, Two-Dimensional Protein Crystals. *Nature* **2016**, 533, 369–373.

- (22) Bailey, J. B.; Zhang, L.; Chiong, J. A.; Ahn, S.; Tezcan, F. A. Synthetic Modularity of Protein—Metal—Organic Frameworks. *J. Am. Chem. Soc.* **2017**, *139*, 8160–8166.
- (23) Strable, E.; Johnson, J. E.; Finn, M. G. Natural Nanochemical Building Blocks: Icosahedral Virus Particles Organized by Attached Oligonucleotides. *Nano Lett.* **2004**, *4*, 1385–1389.
- (24) McMillan, J. R.; Brodin, J. D.; Millan, J. A.; Lee, B.; Olvera de la Cruz, M.; Mirkin, C. A. Modulating Nanoparticle Superlattice Structure Using Proteins with Tunable Bond Distributions. *J. Am. Chem. Soc.* 2017, 139, 1754–1757.
- (25) Cigler, P.; Lytton-Jean, A. K. R.; Anderson, D. G.; Finn, M. G.; Park, S. Y. DNA-Controlled Assembly of a Natl Lattice Structure from Gold Nanoparticles and Protein nanoparticles. *Nat. Mater.* **2010**, *9*, 918–922.
- (26) Tian, Y.; Lhermitte, J. R.; Bai, L.; Vo, T.; Xin, H. L.; Li, H.; Li, R.; Fukuto, M.; Yager, K. G.; Kahn, J. S.; et al. Ordered Three-Dimensional Nanomaterials Using DNA-Prescribed and Valence-Controlled Material Voxels. *Nat. Mater.* **2020**, *19*, 789–796.
- (27) Kostiainen, M. A.; Kasyutich, O.; Cornelissen, J. J. L. M.; Nolte, R. J. M. Self-Assembly and Optically Triggered Disassembly of Hierarchical Dendron-Virus Complexes. *Nat. Chem.* **2010**, *2*, 394–399
- (28) Kostiainen, M. A.; Hiekkataipale, P.; Laiho, A.; Lemieux, V.; Seitsonen, J.; Ruokolainen, J.; Ceci, P. Electrostatic Assembly of Binary Nanoparticle Superlattices Using Protein Cages. *Nat. Nanotechnol.* **2013**, *8*, 52–56.
- (29) Liljeström, V.; Ora, A.; Hassinen, J.; Rekola, H. T.; Nonappa; Heilala, M.; Hynninen, V.; Joensuu, J. J.; Ras, R. H. A.; Törmä, P.; et al. Cooperative Colloidal Self-Assembly of Metal- Protein Superlattice Wires. *Nat. Commun.* **2017**, *8*, 671.
- (30) Künzle, M.; Eckert, T.; Beck, T. Binary Protein Crystals for the Assembly of Inorganic Nanoparticle Superlattices. *J. Am. Chem. Soc.* **2016**, 138, 12731–12734.
- (31) Uchida, M.; McCoy, K.; Fukuto, M.; Yang, L.; Yoshimura, H.; Miettinen, H. M.; Lafrance, B.; Patterson, D. P.; Schwarz, B.; Karty, J. A.; et al. Modular Self-Assembly of Protein Cage Lattices for Multistep Catalysis. *ACS Nano* **2018**, *12*, 942–953.
- (32) Chakraborti, S.; Korpi, A.; Kumar, M.; Stepien, P.; Kostiainen, M. A.; Heddle, J. G. Three-Dimensional Protein Cage Array Capable of Active Enzyme Capture and Artificial Chaperone Activity. *Nano Lett.* **2019**, *19*, 3918–3924.
- (33) Ramberg, K. O.; Engilberge, S.; Skorek, T.; Crowley, P. B. Facile Fabrication of Protein-Macrocycle Frameworks. *J. Am. Chem. Soc.* **2021**, *143*, 1896–1907.
- (34) Zhou, K.; Zang, J.; Chen, H.; Wang, W.; Wang, H.; Zhao, G. On-Axis Alignment of Protein Nanocage Assemblies from 2d to 3d through the Aromatic Stacking Interactions of Amino Acid Residues. *ACS Nano* **2018**, *12*, 11323–11332.
- (35) Zheng, B.; Zhou, K.; Zhang, T.; Lv, C.; Zhao, G. Designed Two- and Three-Dimensional Protein Nanocage Networks Driven by Hydrophobic Interactions Contributed by Amyloidogenic Motifs. *Nano Lett.* **2019**, *19*, 4023–4028.
- (36) Uchida, M.; LaFrance, B.; Broomell, C. C.; Prevelige, P. E., Jr.; Douglas, T. Higher Order Assembly of Virus-Like Particles (Vlps) Mediated by Multi-Valent Protein Linkers. *Small* **2015**, *11*, 1562–1570.
- (37) McCoy, K.; Uchida, M.; Lee, B.; Douglas, T. Templated Assembly of a Functional Ordered Protein Macromolecular Framework from P22 Virus-Like Particles. ACS Nano 2018, 12, 3541–3550.
- (38) Prevelige, P. E.; Thomas, D.; King, J. Scaffolding Protein Regulates the Polymerization of P22 Coat Subunits into Icosahedral Shells in Vitro. *J. Mol. Biol.* **1988**, *202*, 743–757.
- (39) Lander, G. C.; Tang, L.; Casjens, S. R.; Gilcrease, E. B.; Prevelige, P.; Poliakov, A.; Potter, C. S.; Carragher, B.; Johnson, J. E. The Structure of an Infectious P22 Virion Shows the Signal for Headful DNA Packaging. *Science* **2006**, *312*, 1791–1795.
- (40) Zhang, Y.; Ardejani, M. S.; Orner, B. P. Design and Applications of Protein-Cage-Based Nanomaterials. *Chem. Asian J.* **2016**, *11*, 2814–2828.

- (41) Edwardson, T. G. W.; Hilvert, D. Virus-Inspired Function in Engineered Protein Cages. J. Am. Chem. Soc. 2019, 141, 9432–9443.
- (42) Reichhardt, C.; Uchida, M.; O'Neil, A.; Li, R.; Prevelige, P. E.; Douglas, T. Templated Assembly of Organic—Inorganic Materials Using the Core Shell Structure of the P22 Bacteriophage. *Chem. Commun.* **2011**, *47*, 6326.
- (43) Bedwell, G. J.; Zhou, Z.; Uchida, M.; Douglas, T.; Gupta, A.; Prevelige, P. E. Selective Biotemplated Synthesis of Tio2 inside a Protein Cage. *Biomacromolecules* **2015**, *16*, 214–218.
- (44) Lucon, J.; Qazi, S.; Uchida, M.; Bedwell, G. J.; LaFrance, B.; Prevelige, P. E., Jr.; Douglas, T. Use of the Interior Cavity of the P22 Capsid for Site-Specific Initiation of Atom-Transfer Radical Polymerization with High-Density Cargo Loading. *Nat. Chem.* **2012**, *4*, 781–788.
- (45) O'Neil, A.; Reichhardt, C.; Johnson, B.; Prevelige, P. E.; Douglas, T. Genetically Programmed in Vivo Packaging of Protein Cargo and Its Controlled Release from Bacteriophage P22. *Angew. Chem. Int. Edit* **2011**, *50*, 7425–7428.
- (46) Patterson, D. P.; Prevelige, P. E.; Douglas, T. Nanoreactors by Programmed Enzyme Encapsulation inside the Capsid of the Bacteriophage P22. ACS Nano 2012, 6, 5000–5009.
- (47) Jordan, P. C.; Patterson, D. P.; Saboda, K. N.; Edwards, E. J.; Miettinen, H. M.; Basu, G.; Thielges, M. C.; Douglas, T. Self-Assembling Biomolecular Catalysts for Hydrogen Production. *Nat. Chem.* **2016**, *8*, 179–185.
- (48) Brunk, N. E.; Uchida, M.; Lee, B.; Fukuto, M.; Yang, L.; Douglas, T.; Jadhao, V. Linker-Mediated Assembly of Virus-Like Particles into Ordered Arrays Via Electrostatic Control. *ACS Applied Bio Materials* **2019**, *2*, 2192–2201.
- (49) Richardson, J. J.; Cui, J.; Bjornmalm, M.; Braunger, J. A.; Ejima, H.; Caruso, F. Innovation in Layer-by-Layer Assembly. *Chem. Rev.* **2016**, *116*, 14828–14867.
- (50) Tang, Z.; Wang, Y.; Podsiadlo, P.; Kotov, N. A. Biomedical Applications of Layer-by-Layer Assembly: From Biomimetics to Tissue Engineering. *Adv. Mater.* **2006**, *18*, 3203–3224.
- (51) Decher, G. Fuzzy Nanoassemblies: Toward Layered Polymeric Multicomposites. *Science* **1997**, *277*, 1232–1237.
- (52) Servid, A.; Jordan, P.; O'Neil, A.; Prevelige, P.; Douglas, T. Location of the Bacteriophage P22 Coat Protein C-Terminus Provides Opportunities for the Design of Capsid-Based Materials. *Biomacromolecules* **2013**, *14*, 2989–2995.
- (53) Jiang, Z.; Lee, B. Recent Advances in Small Angle X-Ray Scattering for Superlattice Study. *Applied Physics Reviews* **2021**, 8, 011305.
- (54) Wen, A. M.; Steinmetz, N. F. Design of Virus-Based Nanomaterials for Medicine, Biotechnology, and Energy. *Chem. Soc. Rev.* **2016**, *45*, 4074–4126.
- (55) Rother, M.; Nussbaumer, M. G.; Renggli, K.; Bruns, N. Protein Cages and Synthetic Polymers: A Fruitful Symbiosis for Drug Delivery Applications, Bionanotechnology and Materials Science. *Chem. Soc. Rev.* **2016**, 45, 6213–6249.
- (56) Frenkel, D.; Smit, B. *Understanding Molecular Simulation: From Algorithms to Applications*, 2nd ed., Computational Science Series; Academic Press: San Diego, 2001.